

Moiré profilometry using liquid crystals for projection and demodulation

Jan A.N. Buytaert and Joris J.J. Dirckx

*Laboratory of Biomedical Physics, Department of Physics, University of Antwerp
Groenenborgerlaan 171, B-2020 Wilrijk-Antwerpen, Belgium*

Abstract: A projection moiré profilometer is presented in which both projection and optical demodulation are realized with liquid crystal light modulators. The computer generated grids, realized on thin film transistor matrices, allow phase-stepping and discrete grid averaging without the need for any mechanically moving component. Spatial line pitch and phase steps can thus be readily adjusted to suit the measurement precision and object geometry. The device is able to perform topographic measurements with a height resolution of $15\text{ }\mu\text{m}$ on every pixel of the recording device.

© 2008 Optical Society of America

OCIS codes: (120.4120) Moiré techniques; (110.6880) Three-dimensional image acquisition; (230.0250) Optoelectronics.

References and links

1. F. Chen, G.-M. Brown, and M. Song, "Overview of three-dimensional shape measurement using optical methods," *Opt. Eng.* **39**, 10–22 (2000).
 2. R. Martínez-Celorio, J. Dirckx, J. Buytaert, L. M. López, and W. Decraemer, "Modified temporal-phase-unwrapping method for measuring in real time the out-of-plane displacements of the tympanic membrane of Mongolian Gerbil," *Opt. Int. J. Light Electron. Opt.* (in Press doi:10.1016/j.ijleo.2007.05.005) (2007).
 3. J. Dirckx and W. Decraemer, "Optoelectronic moiré projector for real-time shape and deformation studies of the tympanic membrane," *J. Biomed. Opt.* **2**, 176–185 (1997).
 4. M. von Unge, W. Decraemer, J. Dirckx, and D. Bagger-Sjöbäck, "Shape and displacement patterns of the gerbil tympanic membrane in experimental otitis media with effusion," *Hearing Res.* **82**, 184–196 (1995).
 5. M. Takeda, H. Ina, and S. Kobayashi, "Fourier transform profilometry for the automatic measurement of 3-D object shapes," *Appl. Opt.* **22**, 3977–3982 (1982).
 6. W.-H. Su and H. Liu, "Calibration-based two-frequency projected fringe profilometry: a robust, accurate, and single-shot measurement for objects with large depth discontinuities," *Opt. Express* **14**, 9178–9187 (2006).
 7. D. Meadows, W. Johnson, and J. Allen, "Generation of surface contours by moiré patterns," *Appl. Opt.* **9**, 942–947 (1970).
 8. H. Takasaki, "Moiré topography," *Appl. Opt.* **9**, 1467–1472 (1970).
 9. M. Halioua, R. Krishnamurthy, H. Liu, and F.-P. Chiang, "Projection moiré with moving gratings for automated 3-D topography," *Appl. Opt.* **22**, 850–855 (1983).
 10. J. Dirckx and W. Decraemer, "Interferometer for eardrum shape measurement, based on projection of straight line rulings," *Lasers Med. Sci.* **15**, 131–139 (2000).
 11. J. Buytaert and J. Dirckx, "Design considerations in projection phase shift moiré topography, based on theoretical analysis of fringe formation," *J. Opt. Soc. Am. A* **24**, 2003–2013 (2007).
 12. K. Creath, *Progress in optics XXVI*, chap. Phase-shifting interferometry techniques, pp. 357–373 (1988).
 13. J. Wyant, C. Koliopoulos, B. Bhushan, and O. George, "An optical profilometer for surface characterization of magnetic media," *ASLE trans.* **27**, 101–113 (1982).
 14. J. Wyant, "Interferometric optical metrology: basic principles and new systems," *Laser Focus (includes Electro-Optics)* **18**, 65–71 (1982).
 15. J. Dirckx and W. Decraemer, "Grating noise removal in moiré topography," *Opt. Int. J. Light Electron. Opt.* **86**, 107–110 (1990).

16. A. Asundi, *Proc. SPIE vol. 1554B: Second intl conf on photomechanics and speckle metrology: moire techniques, holographic interferometry, optical NDT, and applications to fluid mechanics*, chap. Novel grating methods for optical inspection, pp. 708–715 (SPIE, 1991).
17. A. Asundi and C. Chan, “Phase shifted projection grid - effect of pitch and profile,” *Opt. Lasers Eng.* **21**, 31–47 (1994).
18. C. Quan, C. Tay, X. Kang, X. He, and H. Shang, “Shape measurement by use of liquid-crystal display fringe projection with two-step phase shifting,” *Appl. Opt.* **42**, 2326–2335 (2003).
19. Y. Fujin, H. Xiaoyuan, and S. Wei, “Digital shadow moiré method with phase-shifting based on liquid crystal display projector,” *Acta Optica Sinica* **25**, 1057–1061 (2005).
20. W.-J. Ryu, Y.-J. Kang, S.-H. Baik, and S.-J. Kang, “A study on the 3-D measurement by using digital projection moiré method,” *Opt. Int. J. Light Electron. Opt.* (in Press doi:10.1016/j.jleo.2006.12.016) (2007).
21. J. Dirckx and W. Decraemer, “Coating techniques in optical interferometric metrology,” *Appl. Opt.* **36**, 2776–2782 (1997).
22. J. Dirckx and W. Decraemer, “Automatic calibration method for phase shift shadow moiré interferometry,” *Appl. Opt.* **29**, 1474–1476 (1990).
23. T. Yatagai, M. Idesawa, Y. Yamaashi, and M. Suzuki, “Interactive fringe analysis system: applications to moiré contourogram and interferogram,” *Opt. Eng.* **21**, 901–906 (1982).
24. S. Nakadate, N. Magome, T. Honda, and J. Tsujuchi, “Hybrid holographic interferometer for measuring three-dimensional deformations,” *Opt. Eng.* **20**, 246–252 (1981).
25. W. Osten, *Optical methods in experimental solid mechanics*, chap. Digital processing and evaluation of fringe patterns in optical metrology and non-destructive testing, pp. 308–363 (Springer-Verlag, 2000). Section: Techniques for digital phase reconstruction.
26. B. Drerup, *Optics in biomedical sciences*, chap. Some problems in analytical reconstruction of biological shapes from moiré topograms, pp. 258–261 (Springer-Verlag, 1982).
27. U. Mieth and W. Osten, *Proc. SPIE vol. 1163: Interferometry '89*, chap. Three methods for the interpolation of phase values between fringe pattern skeleton, pp. 151–154 (SPIE, 1989).
28. J. Dirckx and W. Decraemer, “Effect of middle ear components on eardrum quasi-static deformation,” *Hearing Res.* **157**, 124–137 (2001).
29. X. Xie, J. Atkinson, M. Lalor, and D. Burton, “Three-map absolute moiré contouring,” *Appl. Opt.* **35**, 6990–6995 (1996).
30. M.-S. Jeong and S.-W. Kim, “Color grating projection moiré with time-integral fringe capturing for high-speed 3-D imaging,” *Opt. Eng.* **41**, 1912–1917 (2002).

1. Introduction

Grid or structured light projection profilometry is an optical technique which allows to quantify the 3-D shape of surfaces [1]. A grid of straight lines is projected onto the surface of a diffusely reflective object. When this line image is observed under an angle with the projection direction, the lines deform due to the object surface shape, and this deformation can be interpreted as a frequency modulation of the grating pitch. To obtain full field quantitative shape data, essentially two different methods are used for demodulation of these lines and extraction of the height information.

In one scheme, the projected line image is recorded directly, and the demodulation is performed digitally [2-6]. As this method only needs a simple optical setup using a single image, it is fast. However it has the major disadvantage that the camera needs to fully resolve the individual projected grid lines on the object, while the sensitivity depends on grid pitch. High shape accuracy can thus only be obtained using cameras with very high spatial resolution. The gray scale resolution of the camera is also left unused in the demodulation process, as the gray values are only used in the recorded images to locate the position of the lines. In ideal circumstances, a one bit camera would suffice to locate the black and white grid lines (if resolved). To extract the shape information from this kind of images, basically two approaches exist. One is digital moiré interferometry using virtual interference with a computer generated grid [2], or with a pre-recorded reference image in a video frame buffer [3, 4]. Another approach using direct recording of the grid lines is based on frequency domain techniques, which perform Fourier analysis on the deformation of the lines [5, 6]. In any case, at some point in both approaches the image grid lines need to be removed by a type of filtering, at the expense of spatial resolution.

In the other basic scheme for demodulation, the image of the deformed lines is projected onto a second grid, identical to the projection grid, and is referred to as optical moiré interferometry [7-11]. The geometric interference between the deformed and the undeformed grid leads to the formation of so called moiré fringes, which represent contours of equal object height. They can be interpreted as the intersection of the object with a set of subsequent bright and dark planes, called fringe planes which (in the ideal case) have a fixed equidistant fringe plane distance. By changing the relative distance between the projection and observation grating, the phase of the moiré fringes changes, and arctangent methods can be applied to calculate object height from a set of phase shifted moiré interferograms [12-14]. The method needs a more complex optical setup, but it has the major advantage that the camera does not need to resolve the fine projected grid lines, as the demodulation is now performed optically by the second grid: the camera only needs to record the low frequency moiré fringes. In this manner, fine grids can be used to obtain high resolution, even with low spatial resolution cameras. The essential advantage of the method is that the gray scale dimension of the camera is now actively used in the calculation of the shape information. The gray values are not just used to locate the grid lines, but the change in gray scale value between phase shifted moiré fringes is used. The moiré fringes are however superimposed on the remaining fine grid lines, which is called grid noise (cf. Fig. 1(A)). Since the method does not use the image of the grid lines themselves, residual grid noise can be removed by simultaneously translating the projection and observation grating in their own plane [8, 9]. During this translation, the relative distance between the two grids is kept the same, so that the phase of the moiré fringes remains unchanged. This grid averaging can be performed by a continuous motion during continuous acquisition of the moiré interferogram, or by recording the moving grids at discrete instants in time [15]. The result is called a moiré topogram, shown in Fig. 1(B), in which all grid noise is ‘washed’ away. To obtain the phase changes on the one hand, and the grid averaging on the other hand, precise mechanical translation of both grids is needed. In phase-stepping methods phase unwrapping is an inevitable procedure to remove the 2π -phase jumps in order to recover the absolute phase, cf. Fig. 1(C,D).

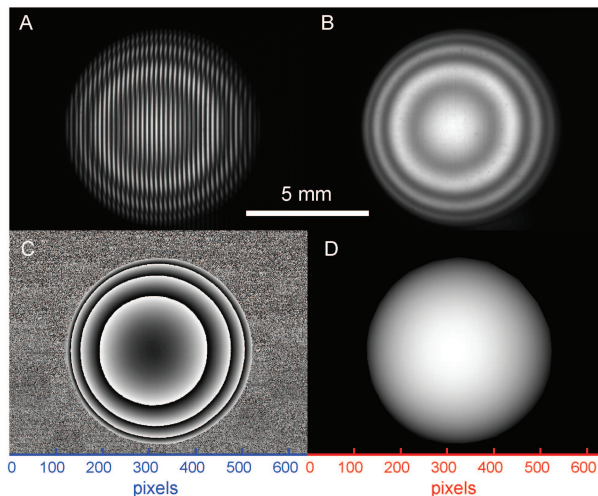


Fig. 1. A: moiré interferogram of a sphere with fringes and grid noise after optical demodulation. B: moiré topogram of the sphere with altitude contour fringes using grid averaging: grid noise is no longer present. E: the 4-bucket phase-stepped algorithm delivers a wrapped phasemap with 2π jumps. F: after unwrapping and calibration a continuous height map is obtained.

Recently, the use of a single liquid crystal light modulator for the projection of the grid lines was introduced [16-20]. This method has the advantage that the grating pitch, and therefore the sensitivity, can be easily adapted to the measurement problem at hand, and allows the implementation of new advanced unwrapping methods based on recordings with different grid pitches. However, this was always combined with digital moiré or Fourier profilometry. We now propose a new technique in which we use two separate liquid crystal light modulating grids, one for projection and one for optical demodulation, and which combines the previously obtained flexibility with the advantages of optical demodulation. With our setup, phase stepping and grid averaging can be realized without any mechanically moving parts. We will discuss the optical design and theoretical background of our method, and demonstrate its capabilities.

2. Device design

2.1. Optical setup

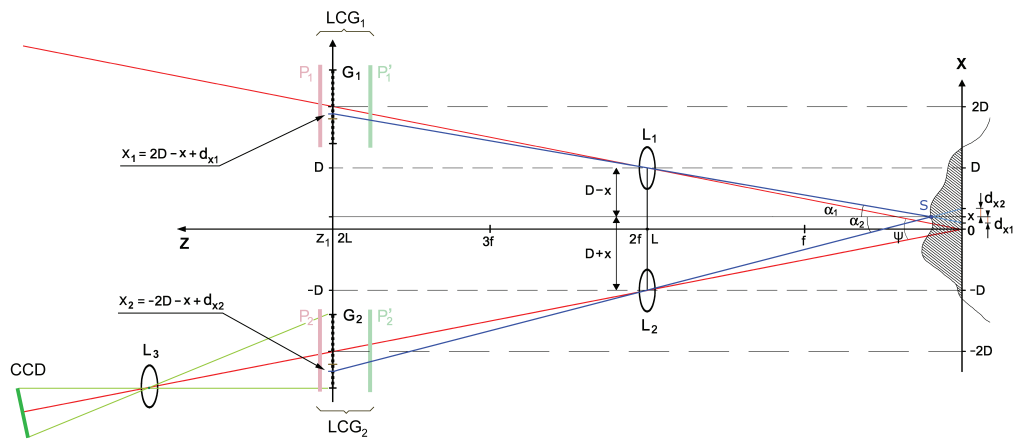


Fig. 2. Schematic layout of the liquid crystal grids setup for projection moiré. Lens L_1 projects the light going through liquid crystal grid unit LCG_1 onto the surface, creating a shadow of grid G_1 on it. The projected line pattern is modulated by the object's geometry, and projected onto grid G_2 of LCG_2 by lens L_2 . The created interferogram is recorded by a CCD imaging device with lens L_3 . A light path from point (x_1, y_1, z_1) on G_1 to surface point $S(x, y, z)$, and from S to (x_2, y_2, z_2) on G_2 is drawn.

The schematic representation of our new projection moiré setup is represented in Fig. 2. Surface height is expressed as distance along the Z-axis. The origin of the coordinate system is chosen in the vicinity of the object's surface (shaded) and on the symmetry axis of the setup. The projection and observation lens, respectively L_1 and L_2 (150 mm Schneider G-Claron f/9), are positioned symmetrically at distance D above and below this axis. The magnification is chosen equal to 1 : 1 by positioning the object and the two grids (G_1 for projection and G_2 for optical demodulation) at distance $L = 2f$ from the lenses. The line grids are formed on 0.7-inch matrices of thin film transistors ($1024 \times 960 p-Si$ TFT contrast ratio 1 : 400), of which the TFT pixels can be controlled separately by a computer. By grouping pixel columns together to form a periodic (square) line grid, a liquid crystal light modulating grid is created. Both liquid crystal light modulators are placed between two linear polarizers with orthogonal polarization direction. When a TFT pixel is fully activated, it rotates the incoming polarized light over 90 degrees. In that case, the light can pass through the second orthogonal polarizer, thus creating a bright transparent pixel. Otherwise when the TFT is inactive, the incoming polarized light is not

rotated and therefore absorbed by the second polarizer, creating a dark pixel. The combination of a TFT grid G_i with its two polarizers P_i and P'_i forms what we will call a liquid crystal based grid (LCG_i). The collimated light source (200W UHP with 2000 lumen) behind LCG_1 is not shown on Fig. 2. A CCD camera (PixelFly PCO 210xs1540) with 640×480 pixels and a 12-bit gray scale range (4096 values) takes an image of the moiré interference pattern on grid G_2 , which contains the interferogram with fringes and grid noise after transmission through LCG_2 . The camera has a macro imaging lens L_3 (50mm Super-Takumar Asahi $f/1.4$) and is positioned along the observation axis, and not orthogonally behind G_2 , to avoid vignetting. This oblique orientation has little influence on the image as the depth of field of the CCD imaging lens covers the entire depth of the grid. A PC software environment created in MATLAB R2007a controls the entire setup: generating the grids on both TFT matrices with the necessary simultaneous or relative pixel shift, taking the CCD-recordings, performing the necessary calculations (see section 2.2) and phase-unwrapping, and finally saving and displaying the three-dimensional surface result.

2.2. Theory

The intensity I_0 of the light source is spatially modulated by LCG_1 , and the modulation pattern is projected by L_1 onto the surface of the object. For simplicity we will assume that G_1 generates a line pattern with a sinusoidal cross section and period p . The transmission of LCG_1 can be written as

$$T_1(x_1) = \frac{1}{2} + \frac{1}{2} \sin\left(\frac{2\pi x_1}{p} + \phi_1\right) \quad (1)$$

with x_1 the position on the X-axis along the grid G_1 and ϕ_1 the initial arbitrary grid phase. In reality we use a square grid transmission profile which can be expressed in sinusoids:

$$T'(x) = \frac{1}{2} + \frac{2}{\pi} \sum_{n=1,odd}^{\infty} \frac{1}{n} \sin\left(\frac{2\pi n x}{p} + \phi_1\right) \quad (2)$$

The higher order components of the resulting intensity profile are however reduced by the limited bandwidth of the projection and demodulation lens, and it has been shown that the presence of the higher orders basically leads to the same result [11].

The projected intensity profile on the surface becomes frequency modulated by the object's shape when observed under an angle ψ . The surface of the object is imaged by lens L_2 onto LCG_2 grid G_2 , which also has period p . Transmission of the light through the liquid crystal grid unit LCG_2 is again described by a multiplication of the light by transmission profile $T_2(x_2) = \frac{1}{2} + \frac{1}{2} \sin\left(\frac{2\pi x_2}{p} + \phi_2\right)$, with x_2 the position along the second grid on the X-axis and arbitrary phase ϕ_2 . The created interferogram is recorded by a CCD. So light from (x_1, y_1, z_1) on G_1 falls on the surface point $S(x, y, z)$ and is reflected onto grid G_2 point (x_2, y_2, z_2) , cf. Fig. 2. The length of this light path is defined $r(x, y, z)$. Transmission through lens L_1 and L_2 create insertion losses ρ_1 and ρ_2 , and the reflectivity $R(x, y)$ on the surface is position dependent. For the intensity I at point $S(x, y, z)$ on the surface, seen by the CCD, we obtain

$$I(x, y, z) = T_2(x_2) \rho_2 R(x, y) \rho_1 T_1(x_1) \frac{I_0}{r^2(x, y, z)} \quad (3)$$

$$\begin{aligned} &= A(x, y, z) \left[\frac{1}{2} + \frac{1}{2} \sin\left(\frac{2\pi(2D - x + d_{x_1})}{p} + \phi_1\right) \right] \\ &\times \left[\frac{1}{2} + \frac{1}{2} \sin\left(\frac{2\pi(-2D - x - d_{x_2})}{p} + \phi_2\right) \right] \end{aligned} \quad (4)$$

with $A(x, y, z) = \frac{I_0 \rho_1 \rho_2 R(x, y)}{r^2(x, y, z)}$ constant during phase shifting. The positions x_1 and x_2 have been substituted in (4) using

$$x_1 = 2D - x + d_{x_1} \quad y_1 = y_2 = -y - d_y \quad (5)$$

$$x_2 = -2D - x - d_{x_2} \quad z_1 = z_2 = 2L = 4f \quad (6)$$

Geometry shows that $d_{x_1} = z \frac{D-x}{L-z}$, $d_{x_2} = z \frac{D+x}{L-z}$ and $d_y = z \frac{y}{L-z}$. Working out expression (4) gives

$$I(x, y, z) = \frac{A}{4} \left\{ 1 + \sin \left(\frac{2\pi(2D-x+z \frac{D-x}{L-z})}{p} + \phi_1 \right) + \sin \left(\frac{2\pi(-2D-x-z \frac{D+x}{L-z})}{p} + \phi_2 \right) \dots \right. \\ \left. + \frac{1}{2} \left[-\cos \left(\frac{2\pi(-2x-z \frac{2x}{L-z})}{p} + \phi_1 + \phi_2 \right) + \cos \left(\frac{2\pi(-4D-z \frac{2D}{L-z})}{p} + \phi_1 - \phi_2 \right) \right] \right\} \quad (7)$$

Note that the second, third and fourth term all have a dependency on x . If we rewrite the second term to

$$\sin \left(\frac{2\pi(2D+z \frac{D-x}{L-z})}{p} + \phi_1 \right) \cos \left(\frac{2\pi x}{p} \right) - \cos \left(\frac{2\pi(2D+z \frac{D-x}{L-z})}{p} + \phi_1 \right) \sin \left(\frac{2\pi x}{p} \right) \quad (8)$$

we notice the $\sin \left(\frac{2\pi x}{p} \right)$ and $\cos \left(\frac{2\pi x}{p} \right)$ factor which can be interpreted as a high-frequency modulation of the light with x . Therefore the second term as well as the third and fourth terms, are interpreted as the grid noise. The last term in Eq. (7) is solely modulated by the object surface height z and causes the bright and dark moiré fringes. We can conclude that the multiplication of the modulated grid lines with the second grid's transmission profile delivers an optical demodulation of the height information.

As stated in the introduction, grating noise can be removed by translating both grids simultaneously. One option is to integrate the recorded light over precisely time $T = \frac{p}{v}$ while moving the grids at constant velocity v over exactly one period p (which is technically difficult and sensitive to errors). The movement of both gratings with speed v can be described by adding a time dependent part to the constant arbitrary phase:

$$\phi_i \rightarrow \phi_i + \frac{2\pi v}{p} t \quad (9)$$

In Eq. (10) and (11) is shown that the second term of Eq. (7) becomes zero for integration time $T = \frac{p}{v}$ (similar for the third and fourth term).

$$\frac{A}{4} \int_0^T \left[\sin \left(\frac{2\pi(2D-x+\frac{D-x}{L-z}+vt)}{p} + \phi_1 \right) \right] dt \quad (10)$$

$$= \frac{pA}{8\pi v} \left[\cos \left(\frac{2\pi(2D-x+\frac{D-x}{L-z})}{p} + \phi_1 \right) - \cos \left(\frac{2\pi(2D-x+\frac{D-x}{L-z}+vT)}{p} + \phi_1 \right) \right] \quad (11)$$

So expression (7) can be reduced to

$$I_T(x, y, z) = \frac{TA(x, y, z)}{4} \left\{ 1 + \cos \left(\frac{2\pi(-4D-z \frac{2D}{L-z})}{p} \right) \right\} \quad (12)$$

with removal of the constant phase offset by defining $\phi_1 - \phi_2 = \frac{2\pi 4D}{p}$. Another option leading to (12), is integrating over a very long period $T \gg \frac{p}{v}$ at constant velocity v until the grid noise falls below the dynamic range of the camera [11].

Both procedures are called continuous grid averaging, which can only be realized by mechanically moving the grids. With our liquid crystal light modulators, grid noise can be removed without any moving part, using discrete grid averaging.

2.3. Discrete grid averaging

To remove grid noise, we now record N static interferograms, each with an extra phase shift Φ for both grids. The transfer function of both grids during the capture of the k -th picture is expressed as

$$T_i(x_i) = \frac{1}{2} + \frac{1}{2} \sin \left(\frac{2\pi x_i}{p} + \phi_i + k\Phi \right) \quad (13)$$

by changing the arbitrary phase of the transmission profiles to

$$\phi_i \rightarrow \phi_i + k\Phi \quad (14)$$

Calculating the interferogram intensity with transmission profile (13), or by simply substituting (14) in (7), the average of all recordings with exposure time T gives us the topogram $I_N(x, y, z)$.

$$\begin{aligned} I_N(x, y, z) &= \frac{TA(x, y, z)}{4N} \sum_{k=1}^N \left\{ 1 + \sin \left(\frac{2\pi (2D - x + z \frac{D-x}{L-z})}{p} + \phi_1 + k\Phi \right) \dots \right. \\ &\quad + \sin \left(\frac{2\pi (-2D - x - z \frac{D+x}{L-z})}{p} + \phi_2 + k\Phi \right) \dots \\ &\quad \left. + \frac{1}{2} \left[-\cos \left(\frac{2\pi (-2x - z \frac{2x}{L-z})}{p} + \phi_1 + \phi_2 + 2k\Phi \right) + \cos \left(\frac{2\pi (z \frac{2D}{L-z})}{p} \right) \right] \right\} \quad (15) \\ &= \frac{TA(x, y, z)}{4} \left\{ 1 + \frac{1}{2} \cos \left(\frac{2\pi (\frac{2zD}{L-z})}{p} \right) \dots \right. \\ &\quad + \frac{1}{N} \sum_{k=1}^N \left[\sin \left(\frac{2\pi (2D - x + z \frac{D-x}{L-z})}{p} + \phi_1 + k\Phi \right) + \sin \left(\frac{2\pi (-2D - x - z \frac{D+x}{L-z})}{p} + \phi_2 + k\Phi \right) \right] \dots \\ &\quad \left. - \frac{1}{2N} \sum_{k=1}^N \cos \left(\frac{2\pi (-2x - z \frac{2x}{L-z})}{p} + \phi_1 + \phi_2 + 2k\Phi \right) \right\} \quad (16) \end{aligned}$$

Equation (12) resurfaces in the first two terms of Eq. (16), again representing the moiré fringes. Notice how it is independent of N and Φ . To make the remaining terms (the grid noise) disappear, we need to pose certain conditions on N and Φ . Let us consider the first noise term, which we can rewrite in the following manner when we assume N even:

$$\frac{TA}{4N} \sum_{k=1}^N \left[\sin \left(\frac{2\pi (2D - x + z \frac{D-x}{L-z})}{p} + \phi_1 + k\Phi \right) \right] \quad (17)$$

$$\begin{aligned} &= \frac{TA}{4N} \sum_{k=1}^{\frac{N}{2}} \left[\sin \left(\frac{2\pi (2D - x + z \frac{D-x}{L-z})}{p} + \phi_1 + k\Phi \right) + \sin \left(\frac{2\pi (2D - x + z \frac{D-x}{L-z})}{p} + \phi_1 + (\frac{N}{2} + k)\Phi \right) \right] \\ &= \frac{TA}{2N} \sum_{k=1}^{\frac{N}{2}} \left[\sin \left(\frac{2\pi (2D - x + z \frac{D-x}{L-z})}{p} + 2\phi_1 + (\frac{N}{2} + 2k)\Phi \right) \cos \frac{N\Phi}{4} \right] \quad (18) \end{aligned}$$

We now see that this noise term will cancel out when $\Phi = \frac{2\pi}{N}(2l+1)$ with $l \in \mathbb{N}$ and $\frac{N}{2} \in \mathbb{N}_0$. The second noise term vanishes in a fully analogous way under the same condition. The third noise term in (16) however does not always disappear under this condition, compare (19) with (18). If we however substitute $\Phi = \frac{2\pi}{N}$ in (19) and make N a multiple of four, after some mathematics we obtain Eq. (20), showing that the final noise term also becomes zero.

$$-\frac{TA}{4N} \sum_{k=1}^{\frac{N}{2}} \left[\cos\left(\frac{2\pi(-2x-z\frac{2x}{L-z})}{p} + \phi_1 + \phi_2 + \left(\frac{N}{2} + 2k\right)\Phi\right) \cos\frac{N\Phi}{2} \right] \quad (19)$$

$$= -\frac{TA}{2N} \sum_{k=1}^{\frac{N}{4}} \left[\cos \left(\frac{2\pi(-2x - z \frac{2x}{L-z})}{p} + \phi_1 + \phi_2 + \frac{3\pi}{2} + 2k\Phi \right) \cos \frac{\pi}{2} \right] \quad (20)$$

To summarize, we have to take $N = 4$ or 8 or 12 or 16 ... images with corresponding phase steps $\Phi = \frac{\pi}{2}$ or $\frac{\pi}{4}$ or $\frac{\pi}{6}$ or $\frac{\pi}{8}$... (or grid pixel shifts $\frac{p_{pix}}{N}$) for both grids in between recordings, to perform discrete grid averaging and to obtain a topogram without grid noise. As we will be performing the simultaneous grid shifts digitally on two liquid crystal grids, the minimal displacement of such a virtual grid is 1 TFT pixel. To extract the height by applying the 4-bucket phase-stepping algorithm (see below), we need four equally spaced relative grid shifts in one grating period, which requires the pixel period p_{pix} of our digital grid also to be a multiple of 4.

Expressed in formulas, we get

$$\Phi = \frac{2\pi}{N}(2l+1) \quad \Delta = \frac{p}{2\pi}\Phi = \frac{p}{N}(2l+1) \quad \Delta_{pix} = \frac{p_{pix}}{N}(2l+1) \quad (21)$$

with $l \in \mathbb{N}$ and $\frac{N}{4} \leq \frac{p_{pix}}{4} \in \mathbb{N}_0$. According to this theory, grid noise can be perfectly removed using just $N = 4$ images in the discrete averaging process. In practice however, common liquid crystal TFT's only have a limited fill factor: In between pixels are inactive zones which remain opaque. During discrete averaging these very fine dark lines can not be made to move, while the formulated theory needs discrete but completely moving gratings. They generate some extra grid noise. The use of more averaging images than 4 is thus needed to diminish the contribution of this fixed line pattern to the image content.

We end up with a measured image $I(x,y,z)$ to which we added an offset term $B(x,y)$ to incorporate background illumination and other undesirable effects:

$$I(x, y, z) = \frac{TA(x, y)}{4} \left[1 + \frac{1}{2} \cos \left(\frac{2\pi \left(\frac{zD}{L-z} \right)}{p} \right) \right] + B(x, y) \quad (22)$$

To extract the height z from (22), we apply the 4-bucket algorithm on four phase-stepped moiré topograms $I_{1 \rightarrow 4}$ with respectively a relative grating shift 0 , $\frac{p}{4}$, $\frac{2p}{4}$ and $\frac{3p}{4}$, each causing an extra phase $\frac{\pi}{2}$:

$$\arctan\left(\frac{I_4 - I_2}{I_3 - I_1}\right) = \frac{4\pi D}{p} \frac{z}{L-z} \approx \frac{4\pi D}{p} \frac{z}{L} \quad (23)$$

with $z \ll L$. This also shows that a full fringe plane distance λ (bright and dark fringe) has been completed every time the height z changes $\frac{pL}{2D}$.

3. Performance and results

We will demonstrate the performance of our moiré device with liquid crystal grids on several objects. A stringent condition for the applicability of a moiré technique is the need for diffusely reflective surfaces. We counter low or direct specular reflectivity by applying a thin layer of magnesium oxide powder (MgO) on the surfaces [21], unless otherwise mentioned.

3.1. Grid noise removal and grid period

From Eq. (23) we obtained the expression for the fringe plane distance $\lambda = \frac{pL}{2D}$ which is directly dependent on period p . Within every λ , the phase (corresponding to the height z) has evolved over 2π and is obtained from gray scale variations within this interval by the arctan method. The number of detectable gray scale values thus determines the number of height steps in each fringe plane distance λ . For a certain camera (e.g. with 4096 gray values) and a certain setup (with fixed L and D), the only way to increase the height sensitivity is by using a smaller pitch p so that the same gray scale range is obtained on a smaller fringe plane interval.

All grids are created digitally by activating groups of TFT pixel columns, thus obtaining liquid crystal light modulators. Each CCD pixel has a measured dimension of $19\text{ }\mu\text{m}$ in object space, and each TFT pixel measures $11.8\text{ }\mu\text{m}$. With liquid crystal computer grids, periods are easier expressed in pixel columns (p_{pix}) than in millimeters (p), which is why we will use p_{pix} from now on. The CCD has a resolution of 640×480 pixels, which in our optical setup corresponds to an image field of $12.2 \times 9.1\text{ mm}$. As the moiré information is demodulated by the second grid, and remaining grid lines are averaged out, the number of CCD pixels only determines the number of objects points on which height is measured.

We tested the grid noise removal theory of section 2.3. Equation (21) states that N images should be taken with both grids shifted over $\Delta_{pix} = \frac{p_{pix}}{N}$ pixels between each recording, and N a multiple of 4, to fully remove the grid noise. As we already explained, the limited fill factor of about 80% of each liquid crystal light modulating pixel also introduces a fine line fixed grid, so more than the minimal theoretical 4 images will be needed to average out all grid noise. The higher the number of averaged images N , the better the grid noise removal will be able to suppress the fine fixed grid. Of course, averaging over more frames takes more time, so we look for an optimized number N without unnecessary increase of measuring time. To determine the optimal number N of frame averagings, we measured the standard deviation of the difference between the measured cross sections through the height profile of a flat plate and the theoretical ideal shape, with systematic distortions removed, for different numbers of averaging steps. Fig. 3 shows these standard deviations obtained from topograms with N averaged images. This standard deviation has two main causes: residual grid noise after grid averaging (caused by the fine fixed grid) and noise of the optical system (electronic noise from the CCD, noise in the background illumination etc.).

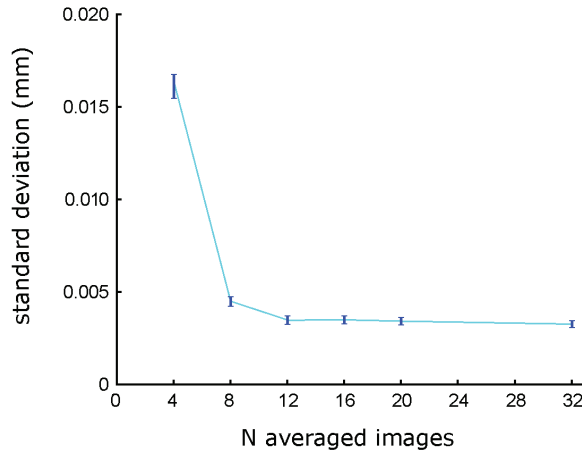


Fig. 3. Standard deviation on height measurements when using the discrete grid averaging theory with N images.

The standard deviation decreases dramatically when going from $N = 4$ to 8. The averaging over 4 images clearly still contains residual grid noise. Using 8 images, results are far better, and with $N = 12$ or 16 the residual grid noise disappears in the measurement noise floor. Once the grid noise is fully removed, standard deviation can be further decreased by increasing the number of averagings. This decrease however evolves only proportionally to the root of the number N , thus demanding many more image recordings (and time) before significant improvements are achieved. Clearly, nothing is gained anymore by using more than $N = 16$ image recordings.

As the LCG's allow easy adaptation of their grid period, an optimal setting can easily be chosen. To demonstrate this, we have used different grid periods p_{pix} in measurements on an oblique flat plate. It was clear that a larger period and therefore a larger fringe plane distance λ , gives rise to fewer phase jump errors, but also lower resolution. In principle, the highest resolution is obtained with the smallest period but, as previously stated, the minimal period p_{pix} has to be at least 4 TFT pixel columns. Throughout this paper we used square gratings, so half of every LCG period p_{pix} is inactive and dark and the other half is transparent. Recordings with periods $p_{pix} = 4, 8, 12, 16, 20, 32$ were taken, and showed that period $p_{pix} = 4$ (consequently combined with the bad discrete grid averaging of $N = 4$) gave a poor result. Four pixel columns form a very high frequency grid (transparent regions of only about $25\mu m$) which are poorly resolved by the projection and demodulation lens. Periods of $p_{pix} = 8$ and more gave good results, also because we then can apply discrete grid averaging of $N = 8$ and more.

All following measurements made with our device are either constructed from $N = 8$ discretely averaged images with period $p_{pix} = 8$ pixel columns, or $N = 16$ with $p_{pix} = 16$ for best image quality. In the latter case, a measurement takes several seconds as 16 images (of in-phase shifted grids) for each of the 4 relative phase shifted topograms have to be recorded.

3.2. Resolution

To obtain the height resolution of our digital moiré device, we made repeated surface recordings of a flat plate using optimal settings, namely $p_{pix} = 16$ and $N = 16$. From the reconstructed surfaces of the flat plate, we compared the center horizontal line with a straight line. Several differences between the measured profile and the theoretical straight line are plotted in the upper part of the graph in Fig. 4. The three plotted curves fall on top of each other and differ less than $\pm 15\mu m$ from the ideal straight line.

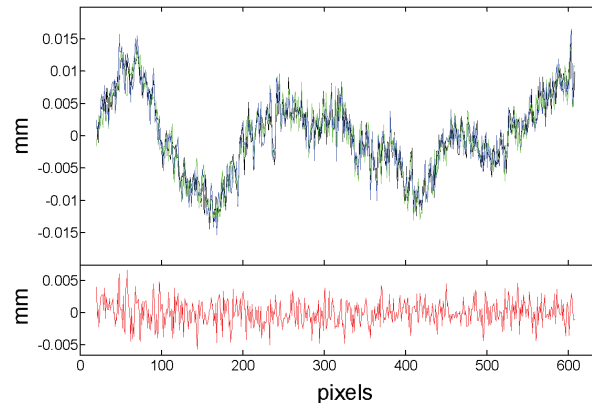


Fig. 4. TOP: difference between the measured profile and an ideal straight plane along a horizontal cross section for three representative measurements. A (systematic) error with amplitude of about $15\mu m$ is present. BOTTOM: difference between two subsequent recorded shape profiles, showing a noise floor of about $5\mu m$.

The curve in the upper part of Fig. 4 shows in every difference curve a low frequency variation, pointing to a systematic error which we will discuss later. If we subtract two subsequent shape measurements, we remove the systematic error and obtain the curve shown in the lower part of Fig. 4. This shows the noise limit of our system, with amplitude $5 \mu\text{m}$.

3.3. Phase versus height calibration and focal depth

In Eq. (23) we obtained the phase from 4 phase shifted images, which can be translated to an altitude z . The conversion factor $\frac{4\pi D}{pL}$ can be calculated from the geometry parameters of the setup, but it is easier and better to calibrate directly by comparing the phase change between two measured surfaces that are shifted over a known distance along Z [22]. By dividing the known physical object shift and the difference of the phase at a certain point, the conversion factor was found to be 0.137 mm/radian for a grid of $p_{pix} = 16$. This means that the distance between two dark or two bright moiré fringes are separated $\lambda = 2\pi \times 0.137 \text{ mm} = 0.858 \text{ mm}$ fringe plane distance apart for $p_{pix} = 16$ pixels. From now on, we will always show calibrated results in millimeters.

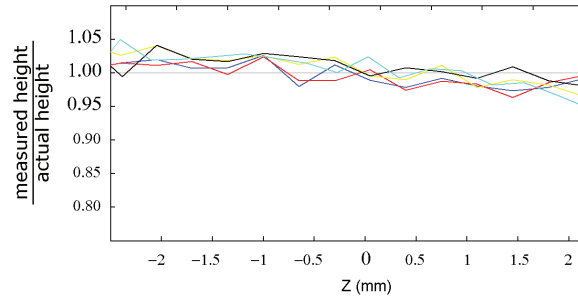


Fig. 5. Ratio of the measured height over the actual mechanical height displacement at Z -steps of $350 \mu\text{m}$ for pixel coordinates $(100,100)$, $(100,550)$, $(240,320)$, $(350,100)$ and $(350,550)$. Deviation of unity is less than 5% over a 5 mm range.

To check linearity of the Z -scaling, we measured the flat plate object positioned at increasing depth steps of $350 \mu\text{m}$ over a distance of several millimeters along Z . The height was determined at the corners and in the center of the image. In Fig. 5 we show the measured height normalized by the actual applied translation, for all five points, as a function of measurement depth. The figure shows that within a range of 5 mm nearly perfect linearity is obtained over the entire imaging field. At the position $z = 0 \text{ mm}$, where the conversion factor was initially determined, the ratio is of course exactly 1 (within the measurement precision). The value for the ratio becomes gradually slightly larger ($< 5\%$) when going 2.5 mm closer to the camera, and slightly smaller going backwards. We will address this in the discussion.

3.4. Spherical objects and difference in reflectivity

As a realistic test object, we used spheres from ball bearings with a measured diameter of 7.99 mm and 15.8 mm . Images at different stages of the moiré topography process for the smallest sphere were already shown in Fig. 1. They lead to the three-dimensional surface presented in Fig. 6. We used $p_{pix} = 16$ and $N = 16$ for all recordings in this section. If we fit a sphere through this (partial) surface, we obtain a radius of 4.09 mm , a deviation of 2.5% from the actual value.

Ideally, the 4-bucket phase-stepping algorithm removes differences in reflected amplitude $A(x,y)$ and background illumination $B(x,y)$, as shown in expression (23). In practice however,

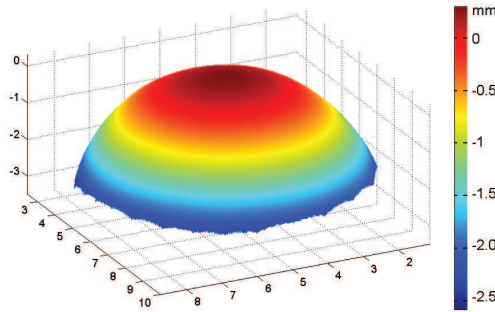


Fig. 6. The 3-D representation of the sphere in Fig. 1 obtained with digital LCD moiré.

slight changes in A and B may occur during the subsequent image recordings which can lead to intensity dependent errors. Even if the lighting and reflection coefficient $R(x,y)$ do not change and A and B remain stable, large differences in $R(x,y)$ might be problematic.

To test the behavior of our moiré method on large differences in reflectivity, the bigger test sphere was not coated homogeneously with MgO , but instead was painted diagonally half in white and half in gray with Chinese ink. A moiré topogram of this surface is shown in Fig. 7(A). In the printed picture, the moiré fringes are barely visible in the dark region, which is also shown in the cross sections plotted in Fig. 7(B). The intensity drops roughly 9 to 10 times between the dark and bright region because of the difference in reflectivity $R(x,y)$, but the height map shown in Fig. 7(C) does not show any artifact. The sphere is perfectly resolved and continued over the dark-bright boundary, demonstrated in the cross sections and 3-D surface in Fig. 7(D) and Fig. 7(E). By using a 12-bit camera, the subtle intensity variations of these fringes are apparently still resolved.

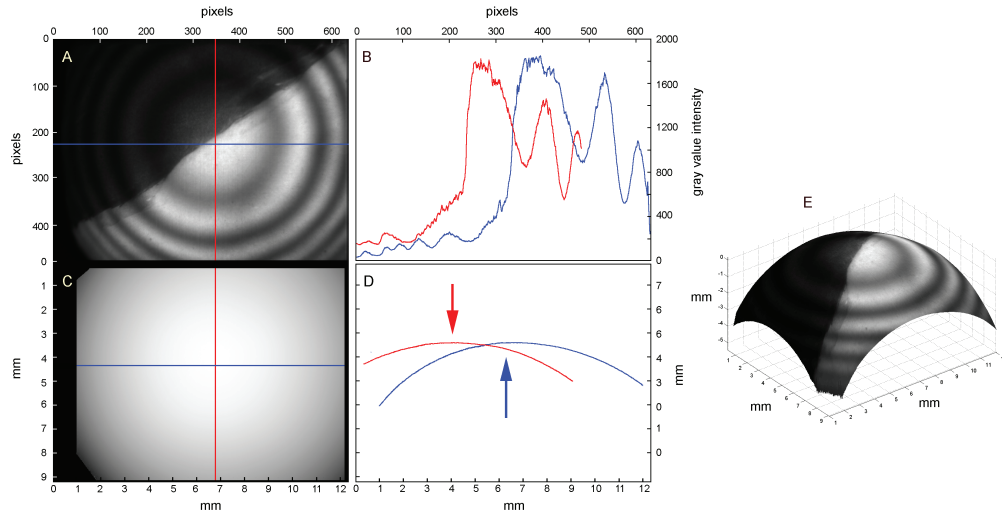


Fig. 7. A: moiré topogram of a diagonally white-gray painted sphere. B: cross sections along the lines in A show $\times 10$ intensity difference between the two regions. C: the differences in reflectivity have no influence on the calibrated height map. D: cross sections along the lines in C, with arrows indicating the bright-dark boundary. E: the 3-D representation of C with one of its topograms mapped on the surface, shows again no problems.

3.5. Fresnel prism

As an application example we measured the topography of a Fresnel prism (Fresnel Optics, Apolda, Germany) which consists of isosceles right-angled triangles of measured height $\beta = 0.49\text{ mm}$ and base width $\gamma = 1.00\text{ mm}$, shown in Fig. 8. The right angles of the steps are well resolved (maximal deviation 2.5%) and the length of its isosceles sides α deviate no more than 0.5% from the real value, indicating that the X - Y - Z calibration of the device is isometric.

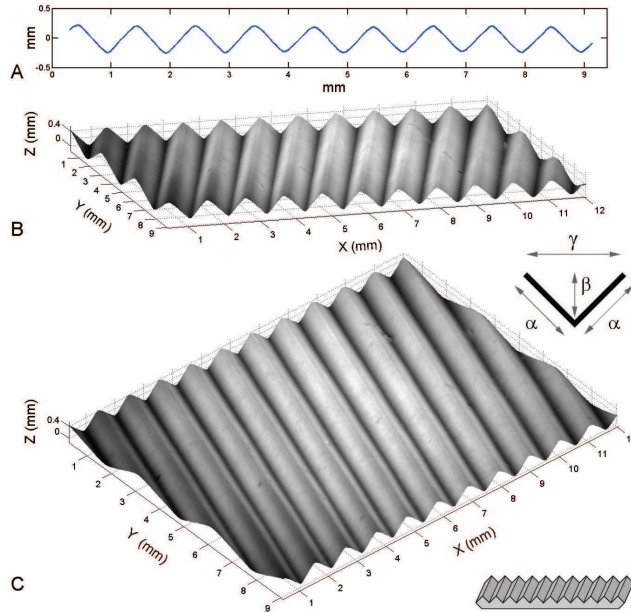


Fig. 8. Triangular Fresnel prism with depth $\beta = 0.49\text{ mm}$ and width $\gamma = 1.00\text{ mm}$. A: cross section through the calibrated height profile shows right-angled isosceles triangles. B and C: 3-D representations of the shape with a topogram mapped on the surface.

4. Discussion

Basically two different methods exist to obtain shape information, each with their specific (dis)advantages. The first type of method, digital moiré and Fourier based techniques, offers simplicity of optical setup and speed, as one only needs to project a single static grid and record a single image. A second grid is not needed, but the projected lines need to be resolved by the camera, so even with a high resolution camera, the grid pitch is limited and inversely related to the height resolution. The fundamental drawback for these techniques lies in the necessary filtering. Digital moiré creates the moiré interferograms by multiplying the single recording with a digital demodulation grid. Grid lines and grid noise still need to be removed from the digitally created fringes by image filtering. These resulting images are typically interpreted by tracing the fringe intensity maxima and minima [23, 24, 25], followed by interpolation between these altitude contours to deliver a height map of the entire surface [25, 26, 27]. The drawback of the Fourier technique also lies in filtering. The object modulates the grid frequency within a certain range. Only this range of frequencies is of interest and is selected in the fourier spectrum. The object shape is then obtained by inverse Fourier transform [5, 6]. As high frequency components are filtered out in digital moiré and Fourier based techniques, this inevitably means the object shape is low pass filtered and steep steps will be smoothed, limiting the in-plane resolution.

The second type of method, used in the present paper, is based on optical demodulation and phase stepping. By using a second grid for optical demodulation, the in-plane resolution of the camera is fully utilized to obtain a height value for every pixel of the recording device without using interpolation or image filtering. The 4-bucket phase-stepping algorithm uses four phase shifted topogram recordings to calculate the object height from the brightness variations in between moiré fringe extremes, independently for every pixel. Even with our modest 12-bit camera of spatial resolution 640×480 pixels, we achieve already an $X-Y$ measuring resolution of $19 \mu m$. The camera also does not need to resolve the grid lines, but only needs to record the moiré interference fringes, which have a low spatial frequency. A smaller grid pitch can thus be applied. The fundamental advantage lies in the fact that the third dimension of the camera, its gray scale range, is used to calculate the height values. The disadvantage of the phase stepping technique is the higher complexity of the setup, since an extra grid is present and both need to be moved in their own plane over exact distances to average out grid noise. Four moiré topograms with different fringe phases are needed for the arctangent method, making phase shifting moiré inevitably slower than the single image direct recording techniques.

Our projection moiré profilometer is based on computer generated grids on liquid crystals for projection and optical demodulation, and performs accurate topographic measurements without any mechanically moving component. Theoretically, the use of liquid crystal grids introduces no new problems to the projection moiré technique, as groups of active and inactive pixel columns can be used to create straight grid lines on the TFT matrices. Combined with orthogonal polarizers, these create the necessary projection and demodulation grid. In practice, the fact that our grids need to be shifted on TFT matrices (simultaneously in-phase for grid noise removal, or relative to each other for phase-stepping with the arctan method), and that the minimal displacement distance is one liquid crystal TFT pixel, puts conditions on the phase shifting and grid period.

The 4-bucket algorithm requires interferograms with fringe phase steps of $\frac{\pi}{2}$ between them, corresponding to $\frac{p}{4}$ relative shifts between the two virtual TFT grids. Therefore the pixel period p_{pix} needs to be a multiple of 4. Good results are obtained with pixel period $p_{pix} = 8$, and even a little better with $p_{pix} = 12$ or 16 or higher. For $p_{pix} = 4$ (line width $\frac{p}{2} \approx 25 \mu m$) the measurements fail because the fine grid lines are not resolved by the projection and demodulation lens.

The discrete grid averaging theory, presented in section 2.3, demands that N interferogram recordings are made, with N also a multiple of four but limited by p_{pix} . The theory states that $N = 4$ would already be sufficient as it fulfills the prescribed theory. This however only holds if the entire grid moves between averaging steps. In reality, a liquid crystal pixel or TFT has a limited fill factor, so a very fine static grid is present which does not move between averaging steps. The relative contribution of this extra grid can only be suppressed by recording more averaging steps. The number of steps needed, depends on the width of the non-active lines: if they are small enough, they will not be resolved by the lenses, broader lines will cause a more pronounced artifact. We therefore measured the residual noise as a function of the averaging number N , cf. Fig. 4. Results obtained with $N = 4$ showed clearly a lower quality than with higher averaging numbers. With discrete averaging of $N = 8, 12$ and certainly 16 recordings all grid noise is washed away and the theory produces moiré topograms with clear fringes. Higher averaging numbers do not significantly improve the measurement quality further.

We obtained a fringe plane distance $\lambda = 0.858 mm$ for TFT pixel column period $p_{pix} = 16$. Avoiding over-exposure and removing the baseline intensity, about 2500 of the 4096 gray values of our camera are applied in the λ interval with the arctan method. This allows for surface reconstruction with a resolution of $15 \mu m$, as shown in section 3.2. This resolution is the same as obtained in conventional moiré techniques (for similar applications) with solid Ronchi rulings [10]. Ronchi grids have a very large contrast ratio while the TFT pixels of the liquid crystal grids

have a limited contrast ratio, typically between 1 : 100 or 1 : 1000. This contrast ratio limits the range of gray scale values, which in turn effects the height measuring resolution. Our resolution can in future work be improved using light modulators with a higher contrast ratio and higher fill factor, eliminating the systematic error and using more dynamic range of the camera.

As we designed our moiré device for measuring the shape and deformation of tympanic membranes of small mammals [4, 28], our imaging field with magnification 1 : 1 corresponds to $12.2 \times 9.1\text{ mm}$. Measurements proved that we maintain a good calibration over the entire image field and over a depth range of 5 mm , cf. Fig. 5. However, as was mentioned in section 3.3, the calibration ratio becomes slightly larger than unity for object points closer to the camera and a little smaller for deeper points, but less than 5% in the depth measuring range of 5 mm . This can completely be attributed to the approximation made in (23) where $\frac{\bar{z}}{L-\bar{z}} \approx \frac{\bar{z}}{L}$. The effect of this compromise is limited, and even can be compensated as is described in [11] in the future. Imaging larger objects is also perfectly possible by changing the setup layout or imaging lenses.

Objects with inhomogeneous reflectivity or different color can be imaged without difficulty. We performed measurements on a gray scale chart with relative density values from a nominal white of 0.05 to 1.95, and found no effect on the measured height. On a painted sphere with an intensity drop of 90% on the surface, the topography showed no artifact, cf. Fig. 7.

It is a challenge to analyze surfaces with lots of discontinuities or complex and steep height differences, especially for correct phase unwrapping. Altitude change between two neighboring CCD pixels is limited to half the fringe plane distance, if standard unwrapping algorithms are to be used (such as our MATLAB function). Several authors proposed solutions for this problem by combining two or more recordings with different pitch into new advanced unwrapping algorithms [6, 20], making it possible to unambiguously unwrap the height maps by comparison and manipulation of the recordings with different height resolution and inter fringe plane distance. Moiré recordings with different grating pitch were previously achieved by physically interchanging the grids, or by ingenious methods like rotating the grid [29], projecting a superposition of several grids in different colors [30], or by encoding the projected grid with two frequencies [6]. With our computerized liquid crystal grids, the implementation of these advanced phase unwrapping algorithms becomes easy and fast, and needs no physical interaction anymore with the optical setup: One simply needs to change the virtual grid in the computer and the LCG's have another pitch with corresponding sensitivity.

5. Conclusion

We presented a projection moiré profilometer which uses liquid crystal light modulators for both projection and demodulation grid. Optical demodulation has the fundamental advantage that the recording camera does not need to resolve individual grid lines, and that high resolution height information is obtained on every image pixel, by using the gray scale sensitivity of the camera and phase-stepping. We realized a setup with projection through and optical demodulation on a TFT matrix, combined with grid noise averaging of discretely moving computer generated grids on liquid crystals. The optical setup was demonstrated with practical measurements, showing a height resolution of $15\mu m$.

The liquid crystal grids offer the advantage over classical fixed grids that the period of the grid can be easily adapted: different height sensitivity adjusted to the object surface geometry can be obtained without any need for physical intervention in the optical setup, and new advanced phase-unwrapping algorithms needing several pitches can be easily implemented.

Acknowledgments

This work was supported by an Aspirant fellowship from the Research Foundation – Flanders (FWO-Vlaanderen). We also thank W. Deblauwe and F. Wiese for their technical assistance.